Electronic Supplementary Material (ESI) for Materials Advances.

Negative thermal expansion triggered anomalous thermal upconverison luminescence behaviors in Er^{3+}/Yb^{3+}-codoped $Y_2Mo_3O_{12}$ microparticles for high sensitive thermometry

Huocheng Lv, Peng Du*, Laihui Luo and Weiping Li

Department of Microelectronic Science and Engineering, School of Physical Science and Technology, Ningbo University, 315211 Ningbo, Zhejiang, China

Corresponding author:

E-mail: dp2007good@sina.com or dupeng@nbu.edu.cn (P. Du)

Table S1. Lattice parameters of $Y_2Mo_3O_{12}$, $Y_2Mo_3O_{12}:Er^{3+}$ and $Y_2Mo_3O_{12}:Er^{3+}/0.22Yb^{3+}$ microparticles.

Parameter	Compounds		
	$Y_2Mo_3O_{12}$	$Y_2Mo_3O_{12}:Er^{3+}$	$Y_2Mo_3O_{12}:Er^{3+}/0.22Yb^{3+}$
Phase	Orthorhombic	Orthorhombic	Orthorhombic
a	13.8688 Å	13.7371 Å	13.6490 Å
b	9.9349 Å	9.9228 Å	9.9261 Å
c	10.0216 Å	9.9512 Å	10.0078 Å
V	1380.82 $Å^3$	1356.44 $Å^3$	1355.85 $Å^3$
$\alpha = \beta = \gamma$	90º	90º	90º
R_{wp}	-	5.47%	5.14%
R_p	-	3.13%	2.97%
GOF	-	1.75%	1.73%

Table S2. CIE coordinates and I_{Green}/I_{Red} value of the $Y_2Mo_3O_{12}:Er^{3+}/0.22Yb^{3+}$ microparticles as a function of temperature.

Temperature	Color coordinate		I_{Green}/I_{Red}
	x	*y*	
303 K	0.274	0.705	13.27
343 K	0.249	0.723	13.16
383 K	0.237	0.732	14.45
423 K	0.229	0.738	15.94
463 K	0.228	0.739	16.59
503 K	0.232	0.735	14.09
543 K	0.233	0.733	13.81
583 K	0.232	0.733	13.66

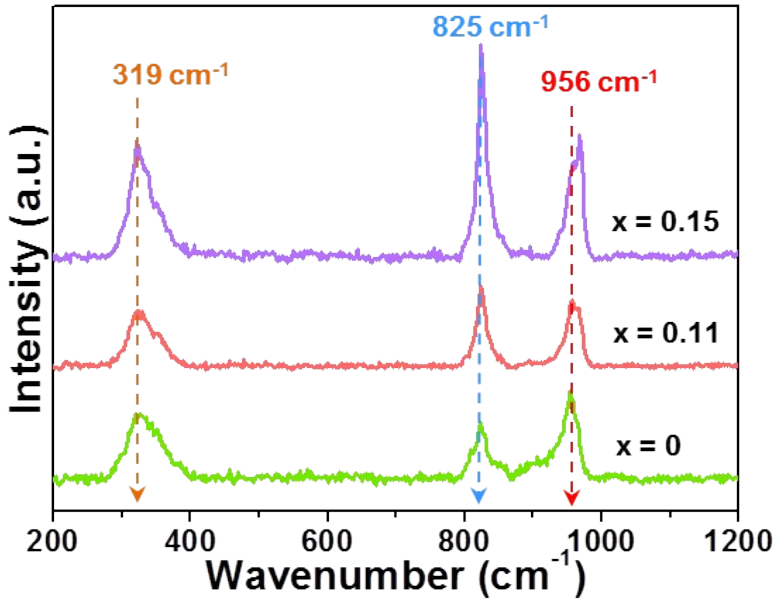

Figure S1. Raman spectra of the $Y_2Mo_3O_{12}:Er^{3+}/2xYb^{3+}$ (x = 0, 0.11, 0.15) microparticles.

The Raman spectra of representative $Y_2Mo_3O_{12}:Er^{3+}$, $Y_2Mo_3O_{12}:Er^{3+}/0.22Yb^{3+}$ and $Y_2Mo_3O_{12}:Er^{3+}/0.30Yb^{3+}$ compounds were measured to get deeper insight into the crystal structure of the studied samples, as shown in Fig. S1. It is seen that all the samples exhibit three featured bands at 319, 825 and 956 cm^{-1} which coincide well with that of the previously reported orthorhombic $Y_2Mo_3O_{12}$.[1,2] Specially, the band at 319 cm^{-1} is assigned to symmetric and asymmetric bending motions in both the YO_6 octahedron and MoO_4 tetrahedron, whereas the peaks at 825 and 956 cm^{-1} are ascribed to symmetric and asymmetric stretching vibrations of the MoO_4 tetrahedra, respectively. Notably, although a secondary phase is observed in the resultant samples when the doping content is 15 mol%, only the Raman modes of orthorhombic $Y_2Mo_3O_{12}$ are seen. This is because that the content of the impurity phase in the prepared is very low.

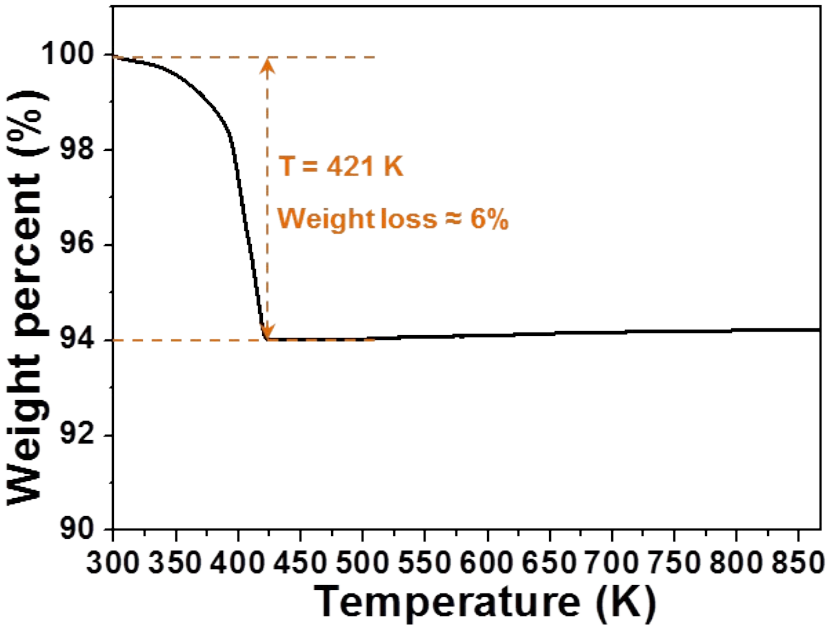

Figure S2. TG spectrum of the $Y_2Mo_3O_{12}:Er^{3+}/0.22Yb^{3+}$ microparticles.

The thermal stability of the studied samples is confirmed by using a TG spectrum. As shown in Fig. S2, one knows that the weight of the samples decrease slowly when the temperature bellows 393 K due to the release of the crystal water which shows weak interaction with $Y_2Mo_3O_{12}$, while it declines sharply when the temperature is over 393 K because of the release of the crystal water with strong interaction with host,[3] leading to a mass decrease of around 6% at 421 K. Clearly, with further increasing the temperature, the mass of the samples do not show any changes. These results suggest that the prepared samples have splendid thermal stability.

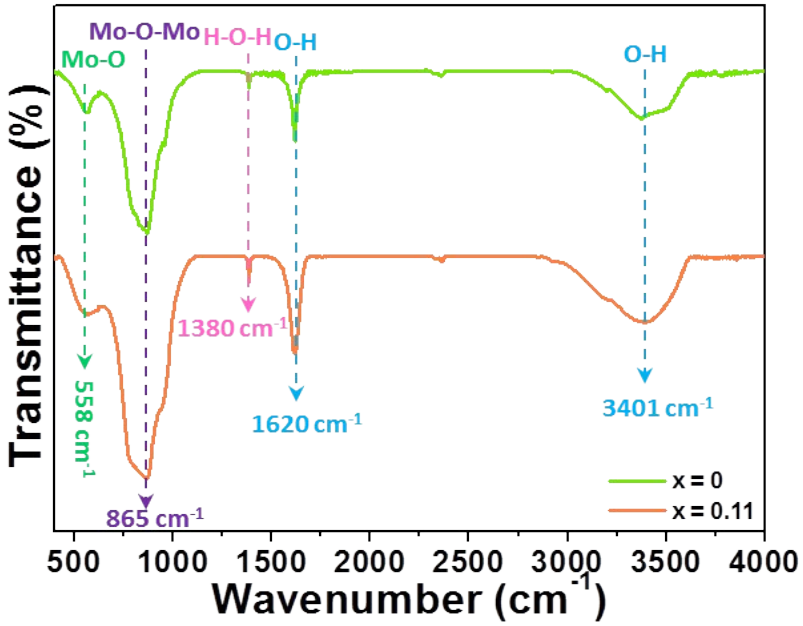

Figure S3. FT-IR spectra of the $Y_2Mo_3O_{12}:Er^{3+}$ and $Y_2Mo_3O_{12}:Er^{3+}/0.22Yb^{3+}$ microparticles.

The surface properties of the final products are verified by using the FT-IR spectrum. The FT-IR spectra of the $Y_2Mo_3O_{12}:Er^{3+}$ and $Y_2Mo_3O_{12}:Er^{3+}/0.22Yb^{3+}$ microparticles are shown in Fig. S3. As disclosed, the bands centered at 3401 and 1620 cm^{-1} corresponding to the stretching vibration of O-H, whereas the peak at 1380 cm^{-1} is attributed to the H-O-H stretching vibration.[4] Furthermore, the band at 865 cm^{-1} is attributed to the Mo-O-Mo vibration mode and the peak located at 538 cm^{-1} is due to the vibration of Mo-O mode.[5]

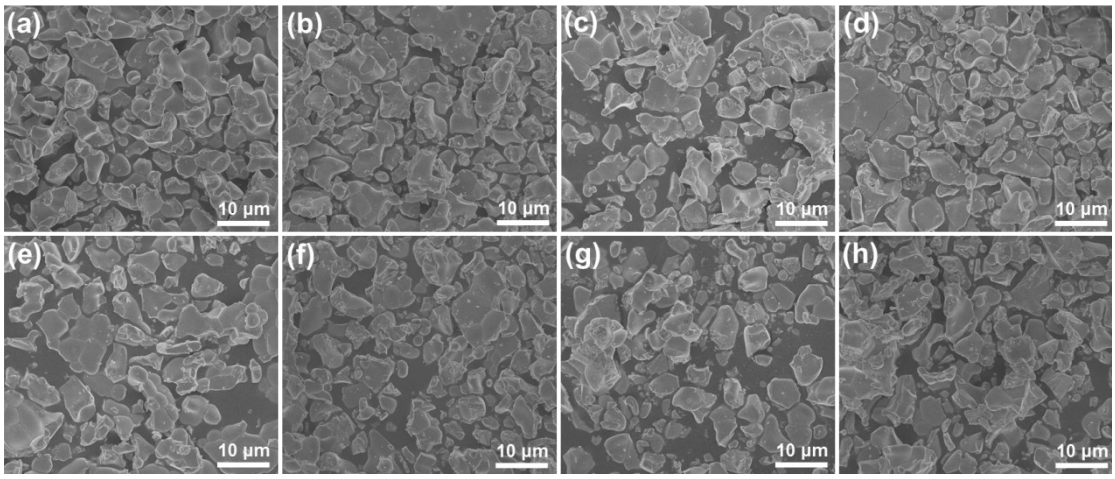

Figure S4. FE-SEM images of the $Y_2Mo_3O_{12}:Er^{3+}/2xYb^{3+}$ microparticles with the doping content of (a) $x = 0$, (b) $x = 0.03$, (c) $x = 0.05$, (d) $x = 0.07$, (e) $x = 0.09$, (f) $x = 0.11$, (g) $x = 0.13$ and (f) $x = 0.15$.

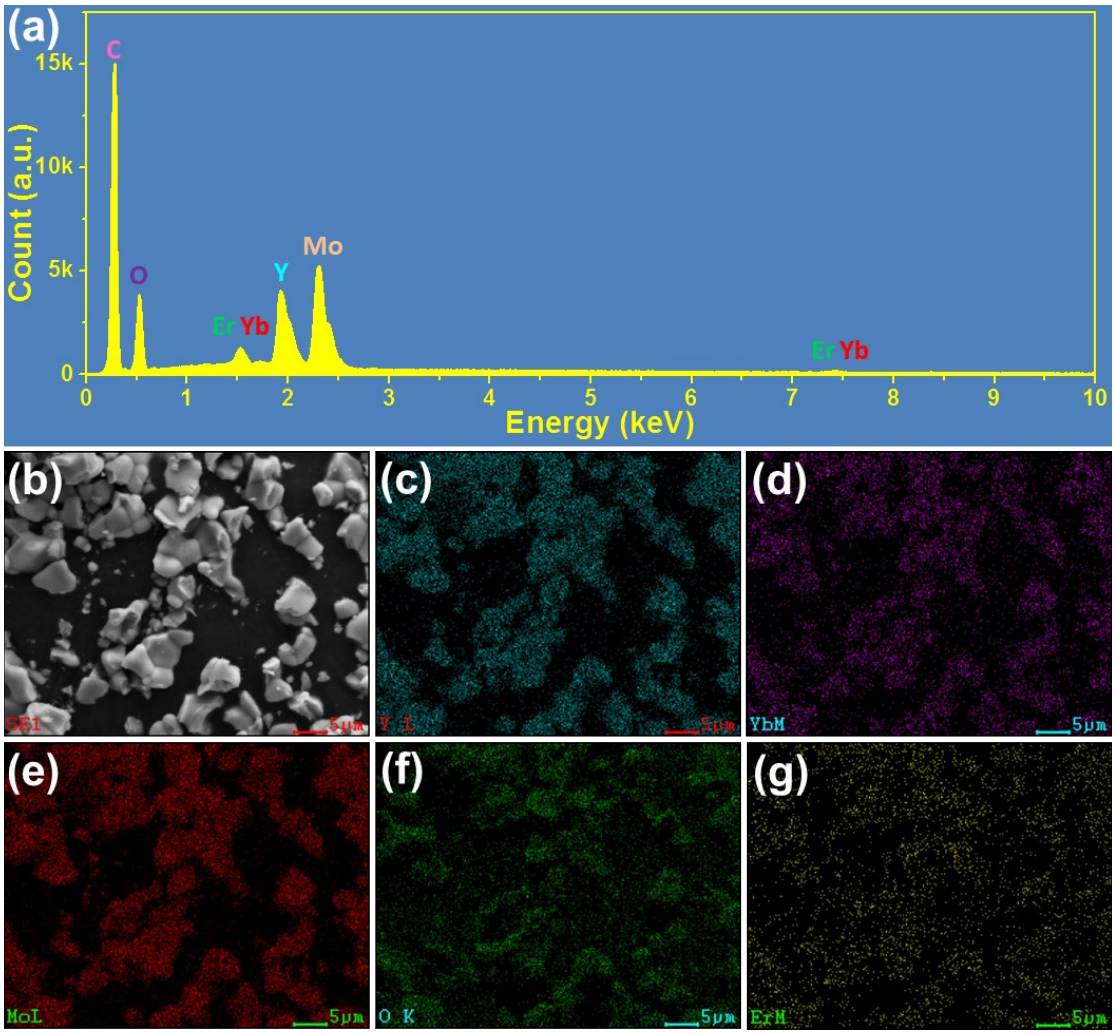

Figure S5. (a) EDS spectrum, (b) FE-SEM image and (c)-(g) Elemental mapping of the $Y_2Mo_3O_{12}:Er^{3+}/0.22Yb^{3+}$ microparticles.

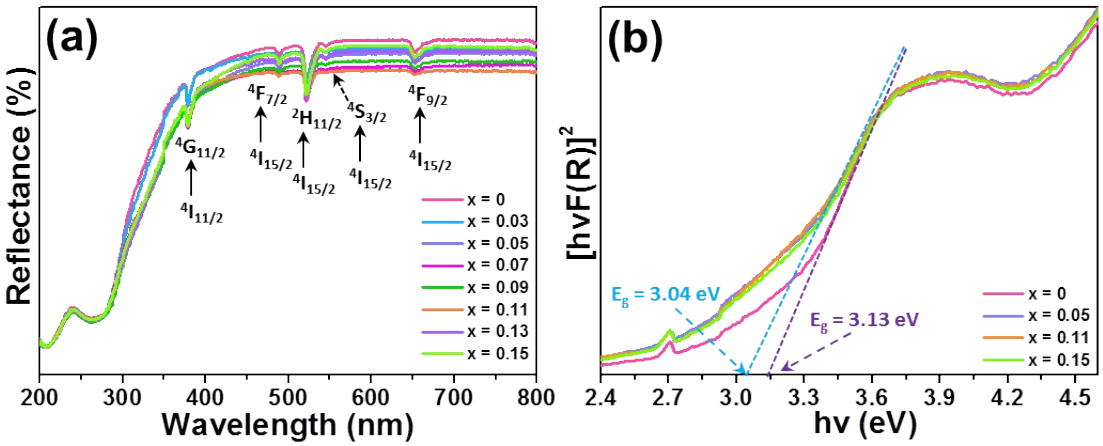

Figure S6. (a) Diffuse reflectance spectra of the $Y_2Mo_3O_{12}:Er^{3+}/2xYb^{3+}$ microparticles. (b) Evaluation of the optical band gap of the $Y_2Mo_3O_{12}:Er^{3+}/2xYb^{3+}$ microparticles *via* the Kubelka-Munk function.

The diffuse reflectance spectra of the $Y_2Mo_3O_{12}:Er^{3+}/2xYb^{3+}$ microparticles in the wavelength range of 200-800 nm were recorded and shown in Fig. S6(a). Significantly, aside from the broad intense absorption band in the range of 200-400 nm arising from the host, there are also five sharp bands originating from the Er^{3+} ions. Specially, these absorption bands at 378, 488, 522, 547 and 652 nm are ascribed to the $^4I_{11/2} \rightarrow {}^4G_{11/2}$, $^4I_{15/2} \rightarrow {}^4F_{7/2}$, $^4I_{15/2} \rightarrow {}^4H_{11/2}$, $^4I_{15/2} \rightarrow {}^4S_{3/2}$ and $^4I_{15/2} \rightarrow {}^4F_{9/2}$ transitions of Er^{3+} ions, respectively.[6] Furthermore, the optical band gap (E_g) of the studied samples can be estimated by using the following expressions:[7,8]

$$\alpha hv = A(hv - E_g)^n, \quad (1)$$

$$F(R) = \frac{(1-R)^2}{2R} = \frac{k}{s}, \quad (2)$$

$$[hvF(R)]^{1/n} = B(hv - E_g) \quad (3)$$

where α is the absorption factor, hv denotes the phonon energy, n = 1/2, 2, 3/2 and 3 shows the direct, allowed indirect, forbidden direct and forbidden indirect electron transition, respectively, A and B refer to the coefficients. Consequently, the E_g values of the studied compounds can be achieved when $[hvF(R)]^{1/n} = 0$. As revealed in Fig. S6(b), when n = 1/2, the fitting results are the best and the optical band gap of the $Y_2Mo_3O_{12}:Er^{3+}/2xYb^{3+}$ microparticles were decided to be around 3.13, 3.04, 3.04 and

3.06 eV, respectively, when the *x* value is 0, 0.05, 0.11 and 0.15. These results suggest that the doping of Yb^{3+} ions has little impact on the optical band gap of the $Y2Mo_3O_{12}$ host.

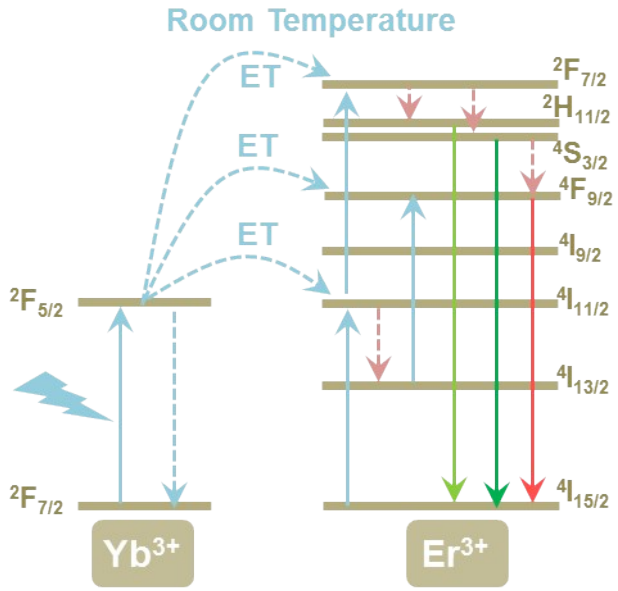

Figure S7. Energy level diagram of the Er^{3+} and Yb^{3+} ions as well as the proposed ET processes at room temperature.

The simplified energy level diagram of Er^{3+} and Yb^{3+} is drawn to explain the UC mechanism in the studied samples, as shown in Fig. S7. Since the Yb^{3+} ions have strong absorption in the near-infrared light and the can efficiently transfer the energy to the Er^{3+} ions, only the energy transfer (ET) from Yb^{3+} to Er^{3+} ions is discussed in present work. As shown, when the samples are excited by 980 nm, the $^2F_{7/2}$ level of Yb^{3+} ions will be pumped to the $^2F_{5/2}$ level. Then the energy will be transferred to the Er^{3+} ions, resulting in the generation of $^4I_{11/2}$ level. At the same time, the second ET from Yb^{3+} to Er^{3+} occurs (*i.e.*, $^4I_{11/2}$ (Er^{3+}) + $^2F_{5/2}$ (Yb^{3+}) → $^2F_{7/2}$ (Er^{3+}) + $^2F_{7/2}$ (Yb^{3+})) and part of the electrons located at $^4I_{11/2}$ level will be excited to $^2F_{7/2}$ level. Afterwards, the non-radiative (NR) transition takes place and the excited levels of $^2H_{11/2}$ and $^4S_{3/2}$ are generated. As a result, the intense green UC emissions are formed owing to the radiative transitions of $^2H_{11/2}$ → $^4I_{15/2}$ and $^4S_{3/2}$ → $^4I_{15/2}$. In contrast, there are two routes to generate the excited levels of $^4F_{9/2}$. As disclosed in Fig. S7, the $^4F_{9/2}$ level is

able to be directly generated from $^4S_{3/2}$ level through the NR transition process. Furthermore, it is worth nothing that electrons at $^4I_{11/2}$ level can also decay to the level of $^4I_{13/2}$ apart from taking part in the generation of $^2F_{7/2}$ level. As for the $^4I_{13/2}$ level, it can be excited to the $^4F_{9/2}$ level through the ET process from Yb^{3+} to Er^{3+} ions. Owing to these two processes, the $^4F_{9/2}$ level is generated, leading to the red UC emissions ($^4F_{9/2} \rightarrow {}^4I_{15/2}$) of Er^{3+} ions.

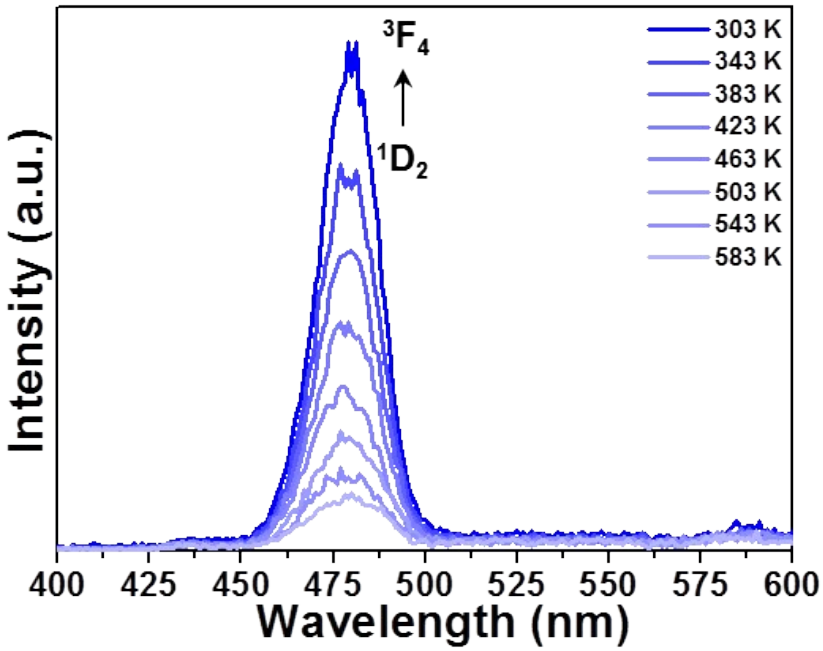

Figure S8. UC emission spectra of the BiOF:Tm^{3+}/Yb^{3+} phosphors as a function of temperature excited at 980 nm.

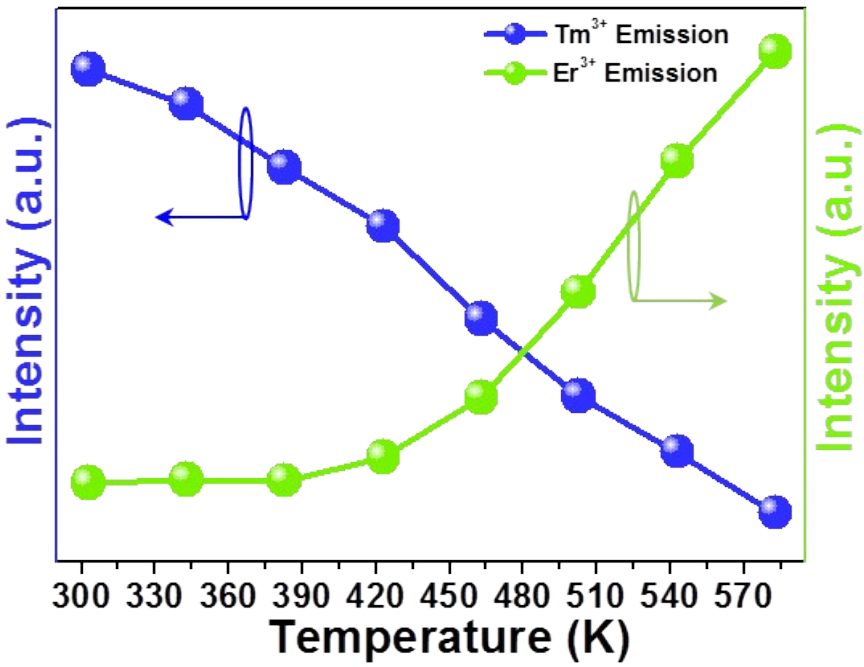

Figure S9. Temperature-dependent emission intensities of Tm^{3+} (*i.e.*, $^1G_4 \rightarrow {}^3H_6$) and Er^{3+} (*i.e.*, $^2H_{11/2} \rightarrow {}^4I_{15/2}$ and $^4S_{3/2} \rightarrow {}^4I_{15/2}$) ions in the designed composites.

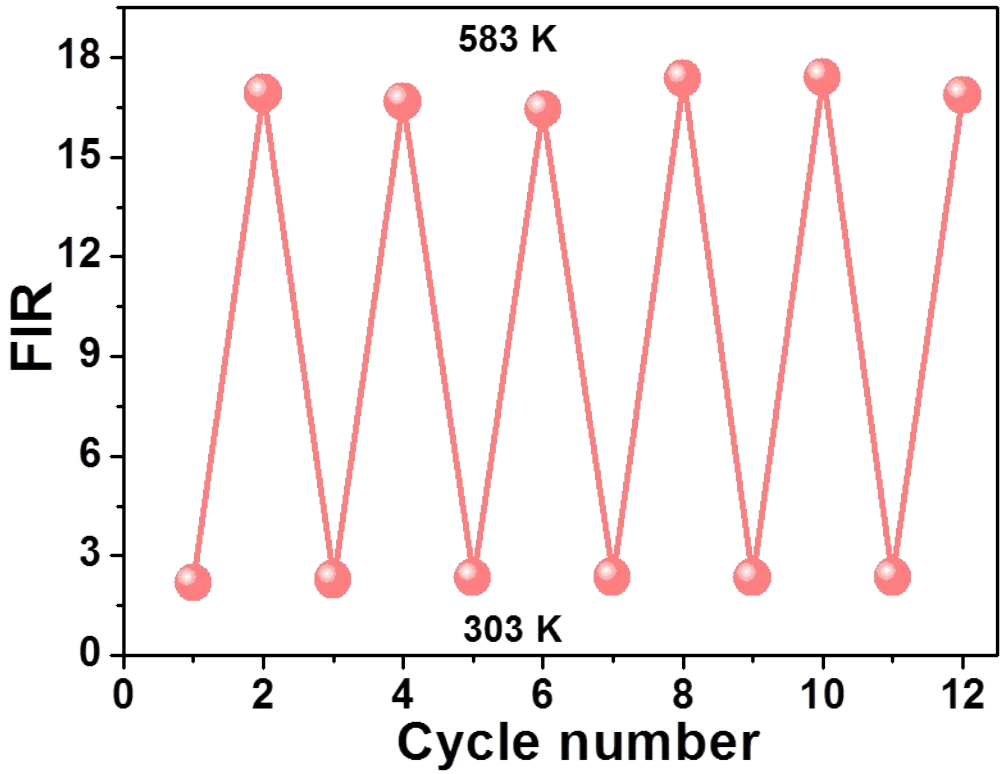

Figure S10. Temperature-induced switching of FIR values of the $Y_2Mo_3O_{12}:Er^{3+}/0.22Yb^{3+}$@BiOF:$Tm^{3+}/Yb^{3+}$ composites in range of 303-583 K.

Reference

1. X. Liu, Y. Cheng, E. Liang, M. Chao, *Phys. Chem. Chem. Phys*. **2014**, 16, 12848-12857.

2. A. C. T. Dias, C. L. Lima, W. Paraguassu, K. P. Silva, P. T. C. Freire, J. M. Filhoa, B. A. Marinkovic, K. J. Miller, M. A. White, A. G. S. Filho, *Vib. Spectros*. **2013**, 68, 251-256.

3. Y. G. Cheng, X. S. Liu, W. B. Song, B. H. Yuan, X. L. Wang, M. J. Chao, E. J. Liang, *Mater. Res. Bull*. **20105**, 65, 273-278.

4. P. Du, J. S. Yu, *Microchm. Acta*. **2018**, 185, 237.

5. X. Zhang, J. Yi, H. Chen, M. Mao, L. Liu, X. She, H. Ji, X. Wu, S. Yuan, H. Xu, H. Li, *J. Eng. Chem*. **2019**, 29, 65-71.

6. R. Adhikari, J. Choi, R. Narro-García, E. DelaRosa, T. Sekino, S. W. Lee, *J. Solid. State. Chem*. **2014**, 216, 36-41.

7. L. Zhou, P. Du, J. S. Yu, *J. Am. Ceram. Soc*. **2019**, 102, 5353-5364.

8. L. Wang, H. M. Noh, B. K. Moon, S. H. Park, K. H. Kim, J. Shi, J. H. Jeong, *J. Phys. Chem. C* **2015**, 119, 15517-15525.